Chinese Chemical Letters 37 (2026) 111542

Contents lists available at ScienceDirect

Chinese Chemical Letters

journal homepage: www.elsevier.com/locate/cclet

Biochar-supported amorphous ferric hydroxide for peracetic acid activation to degrade cefapirin in water: The crucial roles of iron and nitrogen

Han Yan[a], Xudong Yang[b], Wen Liu[b,c], Fengbin Sun[d,*], Guodong Jia[a,*]

[a] College of Soil and Water Conservation, Beijing Forestry University, Beijing 100083, China
[b] The Key Laboratory of Water and Sediment Sciences, Ministry of Education, College of Environmental Sciences and Engineering, Peking University, Beijing 100871, China
[c] Molecular Sciences National Laboratory for Molecular Sciences, Peking University, Beijing 100871, China
[d] Weather Modification Centre, China Meteorological Administration, Beijing 100081, China

ARTICLE INFO

Article history:
Received 7 March 2025
Revised 6 June 2025
Accepted 3 July 2025
Available online 3 July 2025

Keywords:
Peracetic acid
Biochar
Ferric oxyhydroxide
Reactive species
Antibiotics

ABSTRACT

Antibiotic contamination in aquatic environments poses serious risks to ecosystems and public health, necessitating the development of effective removal technologies. In this study, a novel biochar-supported ferric oxyhydroxide (FeOOH/BC) composite catalyst was developed for the activation of peracetic acid (PAA) to degrade cefapirin (CFP), a widely used and persistent cephalosporin antibiotic. The catalyst featured highly dispersed FeOOH nanoparticles and enhanced interfacial electron transfer, enabling efficient activation of PAA through dual pathways involving both radical and non-radical species. FeOOH/BC-1 exhibited the highest catalytic activity, where high-valent iron, singlet oxygen, and surface-bound reactive species played the primary roles in CFP degradation. Fe(III) active sites generate high-valent iron oxo, while N active sites in biochar accounted for the direct electron transfer. This work provides a new approach for activating PAA in the degradation of emerging contaminants and offers a feasible method for catalyst regeneration in wastewater treatment applications.

© 2025 Published by Elsevier B.V. on behalf of Chinese Chemical Society and Institute of Materia Medica, Chinese Academy of Medical Sciences.

Antibiotic contamination in water bodies has become a global concern [1,2]. Antibiotics in aquatic environments can lead to the proliferation of antibiotic-resistant bacteria and the spread of resistance genes, posing potential risks to both ecosystems and human health [3,4]. Therefore, it is an urgent issue to remove antibiotics from water in the field of wastewater treatment. Due to the inhibitory effect of antibiotics on microorganisms, conventional biological treatment processes are often insufficient for their complete removal [5].

Advanced oxidation processes (AOPs), which generate highly reactive oxidative species by activating oxidants, have proven effective in degrading refractory organic pollutants like antibiotics in water [6,7]. Among various AOPs, peracetic acid (PAA)-based AOPs have gained significant attention due to their simple operation, strong oxidation potential, and relatively low toxicity of byproducts [8,9]. The core challenge of PAA-based AOPs lies in the activation of PAA to produce reactive species. Although transition metal ions (*e.g.*, Fe^{2+}, Co^{2+}) can activate PAA, they often cause secondary pollution [8]. To address this, carbon materials are employed as supports for metal ions to enhance stability and reduce metal release [10,11]. Moreover, carbon materials alone can activate PAA through non-radical pathways, but they often exhibit limited reactivity due to low electron transfer efficiency [12,13]. Combining carbon supports with metal ions, particularly iron, offers a promising strategy, providing more active sites, enhancing interfacial charge transfer, and potentially enabling synergistic radical and non-radical activation pathways [14,15]. However, the underlying activation mechanisms of PAA by carbon-supported iron-based catalysts remain insufficiently understood, and most studies to date have not systematically evaluated the structure-activity relationship, catalyst reusability, or performance under environmentally relevant conditions. Thus, it is necessary to investigate the characteristics and mechanisms of PAA activation by carbon-supported metal ion catalysts.

Iron (Fe), a common and environmentally friendly element in the Earth's crust, has minimal ecological risks [16,17]. Due to its multivalent states and strong electron transfer capabilities, iron has been widely used as a catalyst in various reaction systems,

* Corresponding authors.
E-mail addresses: fengbintamu@163.com (F. Sun), jiaguodong@bjfu.edu.cn (G. Jia).

https://doi.org/10.1016/j.cclet.2025.111542
1001-8417/© 2025 Published by Elsevier B.V. on behalf of Chinese Chemical Society and Institute of Materia Medica, Chinese Academy of Medical Sciences.

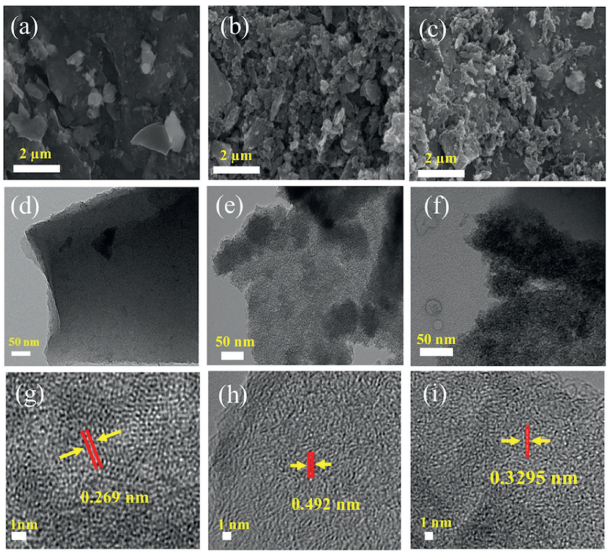


Fig. 1. SEM images of (a) BC, (b) FeOOH and (c) FeOOH/BC-1. TEM images of (d, g) FeOOH/BC-0.5, (e, h) FeOOH/BC-1 and (f, i) FeOOH/BC-2.

such as the activation of hydrogen peroxide and persulfates [18,19]. Among them, ferric oxyhydroxide (FeOOH) has attracted attention due to its abundant surface hydroxyl groups and redox activity, offering the potential to activate PAA effectively. When combined with biochar—a low-cost, renewable carbon material with high surface area and rich surface functionalities—FeOOH can form a stable composite. This composite not only enhances dispersion and prevents metal leaching, but also facilitates interfacial electron transfer during the activation process [20,21]. Cefapirin (CFP), a first-generation cephalosporin antibiotic, is widely used to treat infections in humans and animals [22]. However, CFP discharged into the environment through pharmaceutical and agricultural wastewater is difficult to degrade completely, exhibiting persistence in water. Its presence can disrupt aquatic ecosystems, facilitate the spread of antibiotic resistance genes, and harm microbial communities, threatening aquatic life and public health [23,24].

Based on these challenges, this study developed a novel biochar-supported ferric oxyhydroxide (FeOOH/BC) composite catalyst featuring highly dispersed active sites and enhanced interfacial electron transfer capacity, aimed at efficiently activating PAA to degrade cefapirin (CFP) in water. The FeOOH/BC catalyst enabled a dual-pathway activation mechanism involving both radical and non-radical species, and demonstrated excellent degradation performance, stability, and reusability under environmentally relevant conditions. Furthermore, the degradation pathway of CFP was systematically investigated. The outcomes of this study are expected to provide valuable insights into the rational design of efficient and environmentally friendly catalysts for removing antibiotics in water treatment applications.

Pristine biochar exhibited a rough, flaky surface with abundant irregular pores and crevices, indicative of a hierarchical porous structure favorable for catalyst loading (Fig. 1a). In contrast, the pure FeOOH sample consisted of densely packed nanosheets with irregular morphology, forming aggregated clusters across the surface with limited porosity, which may restrict active site exposure and mass transfer (Fig. 1b). After loading FeOOH onto biochar, the resulting FeOOH/BC-1 composite (number in FeOOH/BC-n mean the dosage of BC) showed that numerous FeOOH nanosheets were dispersed on the biochar surface, partially filling or decorating the existing pores (Fig. 1c). The intimate interface between FeOOH and the carbon matrix suggested enhanced electronic interaction and stability. As the loading increased, a clear aggregation of FeOOH particles was observed, leading to partial pore blockage and surface crowding (Fig. S1 in Supporting information). In addition to scanning electron microscope (SEM) analysis, elemental mapping further confirmed the successful loading and distribution of FeOOH onto the biochar surface (Fig. S2 in Supporting information). The mapping results revealed a uniform distribution of Fe signals across the carbon matrix, indicating that FeOOH was well dispersed rather than localized in large aggregates (Fig. S2b). This homogeneous distribution is essential for maximizing the exposure of active sites and promoting efficient catalytic performance. Transmission electron microscopy (TEM) images revealed that the three materials primarily exhibit a sheet-like morphology, with particle size decreasing as the biochar content in the precursor increases (Figs. 1d-f). The SEM images (Figs. S1a-c) also show that the FeOOH particles become more dispersed and less aggregated as the proportion of biochar in the precursor increases, indicating an improved distribution of active components. No distinct lattice fringes were observed in the images (Figs. 1g-i). X-ray diffraction (XRD) analysis showed a broad peak at a diffraction angle of 22°, indicating the presence of biochar in all three materials (Fig. 2a). The broad diffraction peak centered around 26.2° in the XRD pattern of biochar was typically attributed to the (002) plane of graphitic carbon, indicating a partially ordered graphite-like structure [25]. The additional sharp peaks observed at 20.8° and 28.2° can be attributed to inorganic impurities such as crystalline KCl present in the biochar matrix, which were also detected in the pristine BC [26]. In contrast, pure FeOOH exhibits only weak diffraction peaks at 26.3° and 36.6° (JCPDS No. 18–0639), suggesting that it predominantly exists in an amorphous or poorly crystalline form [27]. This characteristic is retained in the FeOOH/BC composite, where the corresponding peaks remain weak, indicating that the incorporation onto the biochar matrix does not significantly enhance the crystallinity of FeOOH. Moreover, when FeOOH is loaded onto biochar, the porous carbon matrix further inhibits the growth and crystallization of FeOOH particles, as it provides a large specific surface area and abundant anchoring sites that restrict particle agglomeration and long-range ordering. The XRD result is consistent with the TEM results. Compared with pure biochar, the Fourier-transform infrared spectroscopy (FTIR) spectra of the FeOOH/BC composite exhibit several distinct absorption bands, indicating successful incorporation of FeOOH (Fig. 2b). Notably, the bands at approximately 892 cm^{-1} can be assigned to the in-plane bending vibrations of Fe-OH-Fe groups, particularly pronounced in the FeOOH/BC-0.5 sample with higher FeOOH content [28]. Additionally, the absorption band around 1073 cm^{-1} corresponds to Fe-O stretching vibrations, further confirming the presence of iron oxide species. The broadband centered near 3380 cm^{-1}, attributable to O–H stretching vibrations, also differs from that of pristine biochar, reflecting the introduction of hydroxyl–rich FeOOH domains. The thermogravimetric analysis (TGA) curve reveals a distinct weight loss stage occurring between approximately 200–400 °C (Fig. S3 in Supporting information), which can be attributed to the thermal decomposition of FeOOH into Fe_2O_3, accompanied by the release of structural water (-OH groups). Raman spectroscopy showed two prominent peaks at 1353 and 1587 cm^{-1}, corresponding to point defects (I_D) and structural order of carbon materials (I_G), respectively (Fig. 2c). The ratio of I_D to I_G reflects the defect degree [29]. In this study, the defect densities of FeOOH/BC-0.5, FeOOH/BC-1, and FeOOH/BC-2 were 0.86, 0.95, and 0.97, respectively. N_2 adsorption curves showed that the isotherms of FeOOH/BC follow type IV with a pronounced H3 hysteresis loop (Fig. 2d), suggesting that FeOOH/BC is composed of mesoporous materials. The surface area was calculated as 25.2, 10.3 and 15.9 m^2/g, respectively for FeOOH/BC-0.5, FeOOH/BC-1 and FeOOH/BC-2. For the pore diameter distribution, FeOOH/BC-0.5 had no significant peak, and the average diameter is 5.2 nm (Fig. 2e). In comparison, FeOOH/BC-1

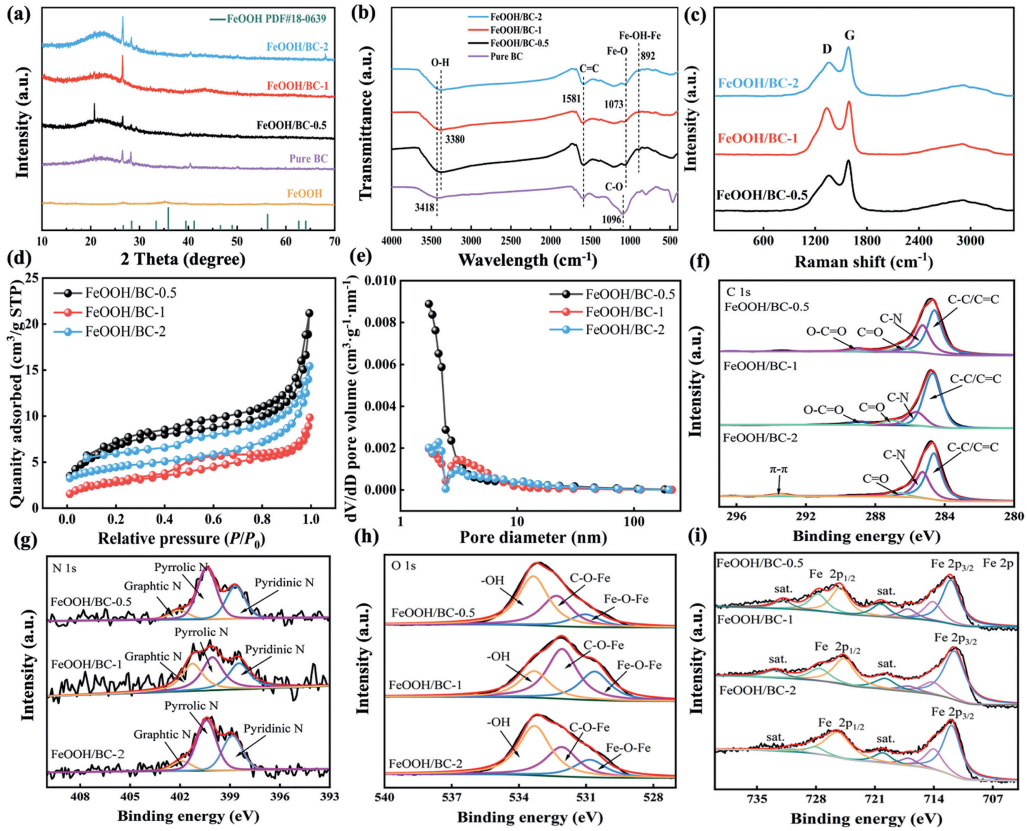


Fig. 2. (a) XRD pattern and (b) FT-IR of materials; (c) Raman spectra, (d) N_2 adsorption-desorption isotherms and pore diameter distribution of FeOOH/BC-0.5, FeOOH/BC-1 and FeOOH/BC-2. High-resolution XPS spectrum (f) C 1 s, (g) N 1 s, (h) O 1 s and (i) Fe 2p.

had one peak at 3.2 nm, further confirming the presence of mesoporous, while FeOOH/BC-2 had two obvious peaks at ~2.1 and ~3.1 nm, suggesting the presence of rich mesoporous.

The X-ray photoelectron spectroscopy (XPS) survey spectra of the three materials revealed the presence of carbon, nitrogen, oxygen, and iron (Fig. S4 in Supporting information). The elemental compositions are summarized in Table S1 (Supporting information), indicating that FeOOH/BC-1 exhibited the highest carbon and iron content, followed by FeOOH/BC-2 and FeOOH/BC-0.5. High-resolution spectra of carbon demonstrated the presence of C–C (284.8 eV), C–N (~285.6 eV), and C–O (~288.0 eV) bonds in all three materials (Fig. 2f) [30]. The nitrogen spectra confirmed the existence of pyridinic nitrogen (~398.8 eV), pyrrolic nitrogen (~399.3 eV), and graphitic nitrogen (~400.5 eV) (Fig. 2g) [31]. Similarly, high-resolution oxygen spectra identified Fe-O (~530.0 eV), C–OH, and H_2O bonds (Fig. 2h) [32]. The Fe 2p XPS spectrum exhibited two distinct binding energy peaks corresponding to Fe $2p_{3/2}$ and Fe $2p_{1/2}$, respectively (Fig. 2i). The energy separation of 13.6 eV between these peaks is indicative of the presence of Fe(III). In the Fe $2p_{3/2}$ region, the peaks at 711.1 eV and 713.1 eV were assigned to Fe(III) species in iron oxide and iron oxide–hydroxide environments, respectively [27]. These features are characteristic of FeOOH. The proportions of the two Fe(III) species in each material are listed in Table S2 (Supporting information), showing that FeOOH/BC-1 has the highest content of the 713.1 eV Fe(III). These characterization results confirm that biochar-supported amorphous FeOOH was successfully synthesized, and the biochar content in the precursor can modulate the FeOOH content and coordination structures.

Biochar (BC) alone showed limited capacity for CFP removal, achieving only an 8.9 % removal rate after 30 min (Fig. 3a). Meanwhile, PAA alone exhibited only a limited degradation efficiency (~13.7 %), suggesting that its contribution to CFP removal is negligible. However, the removal rate of CFP significantly increased (~100 %) when FeOOH/BC was added, indicating that FeOOH/BC effectively activates PAA (Fig. 3a). $HClO_4$ was used to adjust pH due to its complete dissociation into inert ClO_4^- ions, which are non-reactive in advanced oxidation systems, and control experiments without $HClO_4$ confirmed that its presence had no significant impact on CFP degradation efficiency (Fig. S5 in Supporting information). The degradation of CFP follows *pseudo*-first-order kinetics (Fig. S6 in Supporting information), with the rate constants for FeOOH/BC-0.5, FeOOH/BC-1, and FeOOH/BC-2 being 0.20, 0.26, and 0.24 min^{-1}, respectively. The differences in the rate constants among FeOOH/BC-0.5, FeOOH/BC-1, and FeOOH/BC-2 are not substantial. This limited variation may be attributed to the combined effects of Fe content and the nature of the electron transfer process. Specifically, although higher Fe loading can enhance catalytic activity, the overall reaction rate may still be governed by the relatively slow electron transfer mediated by the biochar component. The degradation rate is lower than that reported in the previous study, but in their study, the high concentration of PAA (50 μmol/L) and lower concentration of CFP (2 mg/L) were used (Table S3 in Supporting information) [33]. Since FeOOH/BC-1 had the fastest rate constant, FeOOH/BC-1 was selected for subsequent experiments. Increasing the concentration of PAA accelerated the removal of CFP (Fig. 3b). The lack of further enhancement in CFP degradation rate upon increasing the PAA concentration to 100 μmol/L may be due to the limited number of active sites on the catalyst surface. Excess PAA cannot be effectively activated to generate additional reactive species, leading to a plateau in degradation efficiency. At a PAA concentration of 80 μmol/L, 5 mg/L CFP could be completely degraded in 10 min, which was twice as fast as when the PAA concentration was 10 μmol/L. This is because a higher PAA concen-

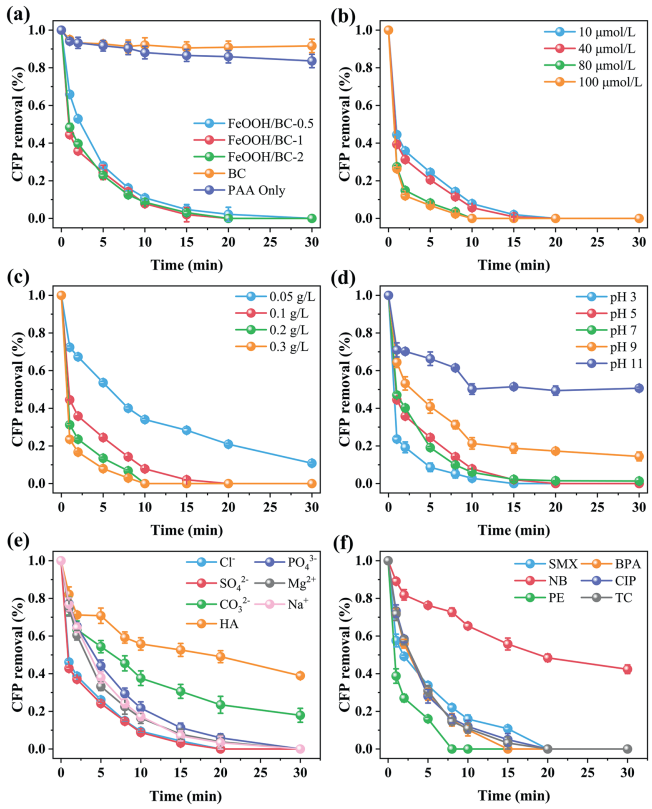


Fig. 3. (a) CFP degradation kinetics by FeOOH/BC/PAA system. (b) Effect of PAA initial concentration. (c) Effect of FeOOH/BC dosage. (d) Effect of solution pH. (e) Effect of inorganic ions and humic acids. (f) Degradation of other recalcitrant organic pollutants. Experimental conditions: [CFP] = 5 mg/L, [PAA] = 10 μmol/L, [FeOOH/BC] = 0.1 g/L, temperature = 27 °C.

tration increases the concentration of active species generated in the system, thus speeding up CFP degradation. Similarly, increasing the amount of FeOOH/BC-1 also accelerated CFP degradation (Fig. 3c), primarily due to the increase in active sites, which enhanced the activation rate of CFP. The removal efficiency of CFP in the FeOOH/BC-1/PAA system decreased with an increase in pH (Fig. 3d). FeOOH/BC-1 has a zero-point of charge at pH 7.2 (Fig. S7 in Supporting information), and when the pH is greater than 7.4, the surface becomes negatively charged, which repels PAA molecules and significantly reduces the removal efficiency of CFP [34]. At pH 3, the degradation rate of CFP was significantly faster than at pH 5 and 7, likely because acidic conditions promoted the conversion of Fe^{3+} to Fe^{2+} [35], and also facilitated the activation of PAA. In contrast, under high pH conditions, some PAA decomposed into acetic acid and hydrogen peroxide [36], which reduced the concentration of generated reactive species.

Chloride (Cl^-) and sulfate ions (SO_4^{2-}) in water did not significantly affect the degradation of CFP in the FeOOH/BC-1/PAA system, but CO_3^{2-} ions and humic acid significantly reduced the removal efficiency of CFP (Fig. 3e). The inhibition by CO_3^{2-} may be due to an increase in solution pH or the complexation of iron active sites, while humic acid may inhibit CFP removal by competing for reactive species. The trivalent PO_4^{3-} exhibited an inhibitory effect on the degradation of CFP. This is likely due to its strong complexation ability with metal ions, which reduces the availability of catalytic species necessary for PAA activation. Overall, the FeOOH/BC-1/PAA system shows excellent resistance to the interference of inorganic ions. It not only effectively degrades CFP, but also efficiently degrades other refractory organic pollutants (Fig. 3f). The reaction system exhibited high removal efficiencies toward typical antibiotics such as sulfamethoxazole (SMX), ciprofloxacin (CIP), and tetracycline (TC), achieving complete degradation within 20 min. Additionally, phenol (PE) and bisphenol A (BPA) were completely removed within 10 and 20 min, respectively, while the removal rate of nitrobenzene (NB) reached 57.7 % within 30 min. The differences in degradation rates may be attributed to the varying reactivities of pollutant-specific functional groups with reactive species.

To investigate the mechanism of FeOOH/BC-1 activating PAA, quenching experiments were first performed to verify the types of active species generated in the system. *Tert*–butyl alcohol was used to quench hydroxyl radicals ($HO^•$), ethanol was used to quench $HO^•$, $CH_3C(=O)OO^•$, and $CH_3C(=O)O^•$, while furfuryl alcohol was used to quench singlet oxygen ($^1O_2$) [33,37]. The results, shown in Fig. 4a, indicate that the addition of *tert*–butyl alcohol had no significant inhibition, suggesting that $HO^•$ has a weak presence in the system. After adding ethanol, there was a slight inhibition after 30 min, with the CFP removal rate around 95 %, indicating that $CH_3C(=O)OO^•$ and $CH_3C(=O)O^•$ contribute minimally. After adding furfuryl alcohol, the degradation rate of CFP slowed down, with a CFP removal rate of about 82.9 % after 30 min. To further confirm the role of $^1O_2$, NaN_3 was added as a quencher (Fig. 4a). The degradation efficiency showed negligible inhibition, indicating that $^1O_2$ contributed minimally to the degradation process. The addition of KI effectively inhibited the degradation of CFP, indicating the involvement of surface-bound oxidative species, such as high-valent iron species. The contribution of high-valent iron-oxo species was further verified using phenyl methyl sulfoxide (PMSO) as a probe compound [38]. With increasing reaction time, the concentration of phenyl methyl sulfone ($PMSO_2$) gradually increased, and the conversion rate of PMSO to $PMSO_2$ reached approximately 25 %, suggesting the participation of high-valent iron species in the degradation of CFP (Fig. 4c). Considering the potential role of carbon-material-mediated direct electron transfer (DET), dichromate ($Cr_2O_7^{2-}$) and benzoquinone (BQ) were introduced into the reaction system as electron acceptors. Upon the addition of dichromate, the degradation efficiency of CFP decreased significantly from 100 % to 38.4 %, indicating the involvement of a DET pathway in CFP degradation. Similarly, the presence of BQ also suppressed the degradation of CFP. In addition, N_2 purging was conducted to exclude the contribution of superoxide radicals (Fig. S8 in Supporting information), further supporting the DET mechanism. Electron paramagnetic resonance (EPR) spectroscopy was further employed to identify the active species in the system. When DMPO was used as a spin-trapping agent, no significant active species signals were observed, confirming the contribution of $HO^•$. However, when TEMP was used as the spin-trapping agent, a clear signal of the triplet state appeared, confirming the presence of singlet oxygen, attributed to the transformation of other reactive species (Fig. 4b). Electrochemical tests were conducted to confirm the formation of surface-active species further. Cyclic voltammetry showed that the current significantly increased upon adding PAA and CFP, with notable redox peaks (Fig. 4d), indicating that PAA and CFP underwent redox reactions on the surface of FeOOH/BC-1 [39]. Open circuit potential measurements showed that the potential significantly increased after adding PAA (Fig. 4e), suggesting that PAA transferred electrons to FeOOH/BC-1 [40]. When CFP was added, the potential decreased, indicating that FeOOH/BC-1 transferred electrons to CFP [41]. These results further confirm the formation of surface-active species in the FeOOH/BC-1/PAA system and their subsequent electron transfer with CFP.

To further evaluate the stability of the catalyst, we conducted post-reaction characterization, including SEM, XRD, and XPS analyses. SEM images (Fig. S1d) show that the catalyst surface becomes rougher after the reaction, indicating the interface reactions. Elemental mapping (Fig. S2c) confirms that Fe remains uniformly distributed on the surface, consistent with the fresh catalyst. More-

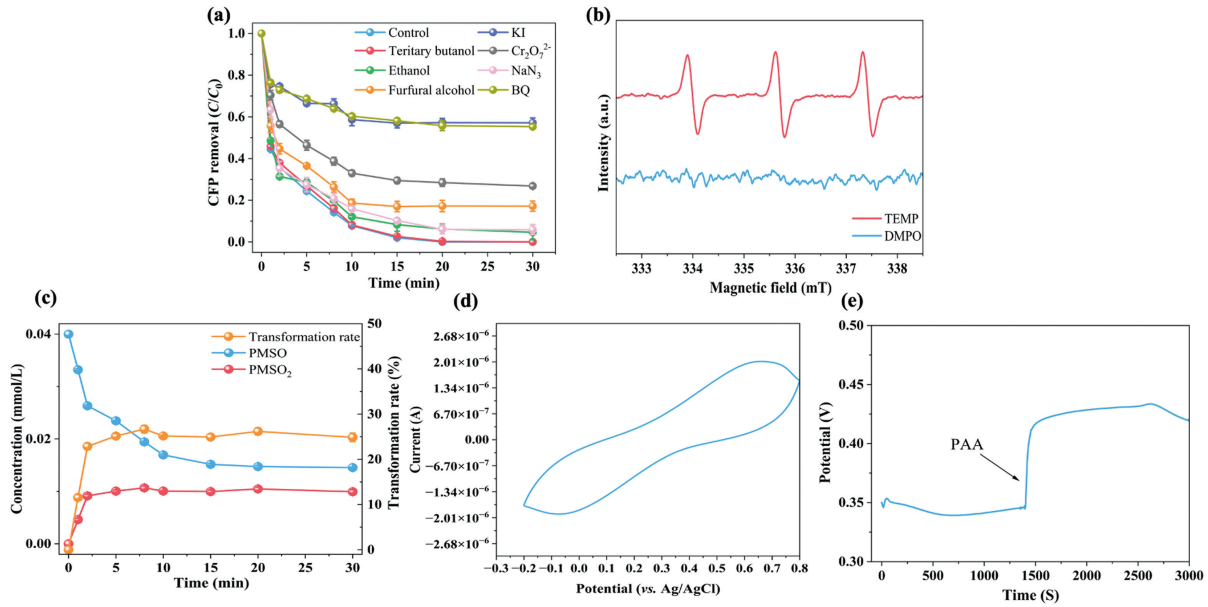


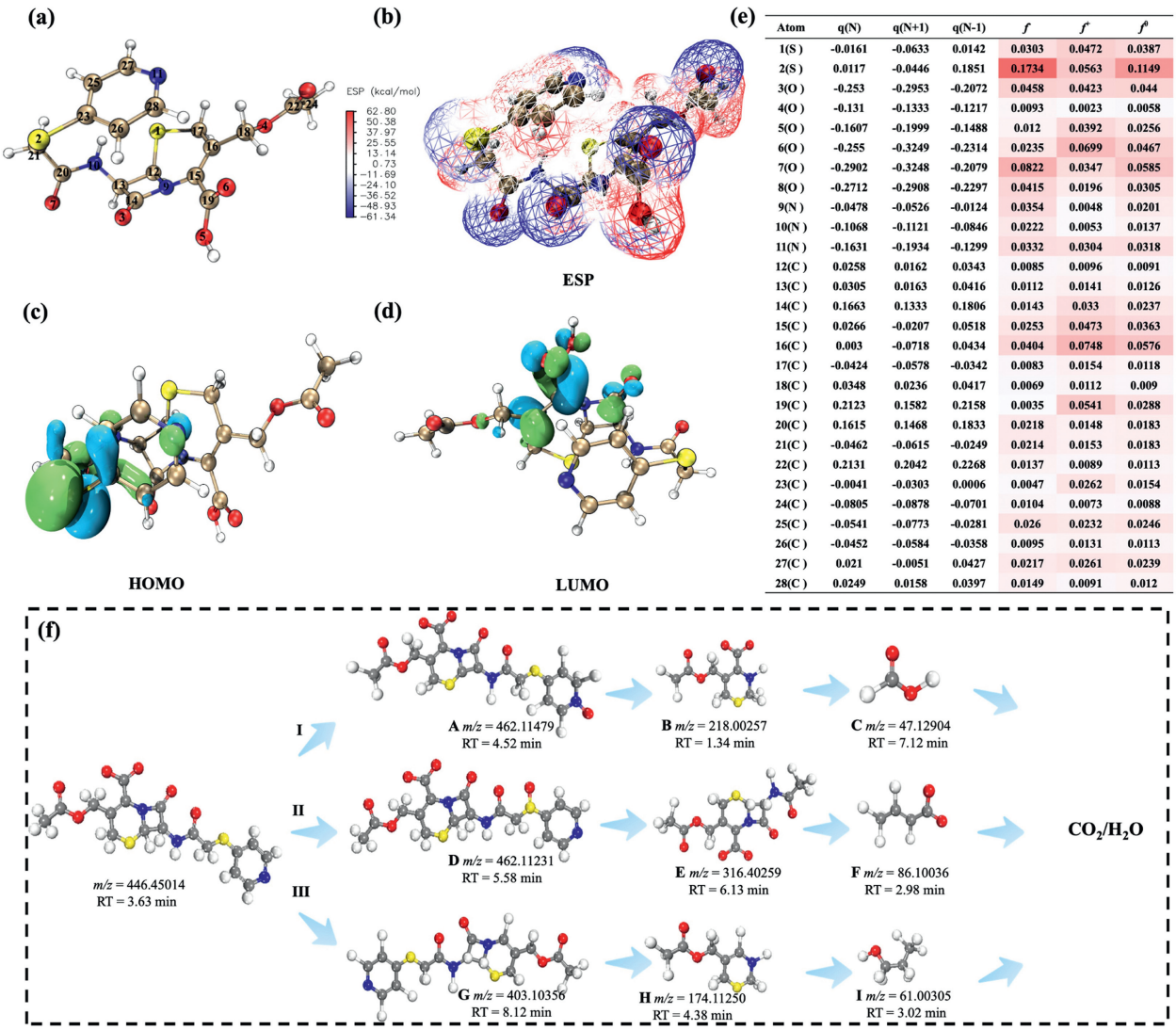
Fig. 4. (a) CFP degradation with different scavengers. (b) EPR spectra of TEMP $^1O_2$. (c) PMSO degradation and $PMSO_2$ formation. (d) Cyclic voltammetry experiments. (e) Open-circuit voltage experiment. Experimental conditions: [CFP] = 5 mg/L, [PAA] = 10 μmol/L, [FeOOH/BC] = 0.1 g/L, [PMSO] = 40 μmol/L, [*tert*–butanol] = [ethanol] = [furfural alcohol] = 4 mmol/L, [KI] = [$K_2Cr_2O_7$] = [NaN_3] = [BQ] = 1 mmol/L.

over, the XRD pattern (Fig. S9 in Supporting information) shows no new diffraction peaks after the reaction, suggesting that the crystalline structure of the catalyst remains stable. The changes in the oxidation states of elements before and after the reaction were analyzed (Fig. S10 in Supporting information), as shown in Table S4 (Supporting information). The composition of all elements did not change before and after the reaction. For the carbon element, the proportion of C–C components decreased after the reaction, while the proportion of C–O components increased. This increase in the proportion of C–O was due to the adsorption of CFP and its intermediates onto FeOOH/BC. The binding energy of all carbon components remained unchanged (Fig. S10a), suggesting that carbon materials did not directly participate in the activation of PAA during the reaction. The proportion of pyridine N and pyrrole N increased after the reaction, while the proportion of graphitic N decreased. This change was attributed to the adsorption of CFP and its intermediates onto FeOOH/BC. The binding energies of pyridine N, pyrrole N, and graphitic N all increased after the reaction (Fig. S10b), indicating that nitrogen acted as an electron donor in the activation of PAA [42]. The proportions of Fe-O bonds and C–O bonds decreased after the reaction, while the proportion of adsorbed H_2O increased. This was due to the adsorption of H_2O during the reaction on FeOOH/BC. The binding energy of Fe-O bonds increased after the reaction (Fig. S10c), indicating that lattice oxygen participated in the activation of PAA [43]. The proportion of FeOOH at 711.1 eV decreased after the reaction, while the proportion of Fe(III) assigned to Fe-OOH at 713.1 eV increased (Fig. S10d), suggesting the transformation process of Fe-related species. The binding energies of both Fe(III) types decreased after the reaction, indicating that both Fe(III) types acted as electron acceptors in the activation of PAA [44]. In addition, the Fe content is directly proportional to the catalytic activity of FeOOH/BC with a correlation coefficient of 0.91 (Fig. S11 in Supporting information). The proportion of Fe(III) at around 711.1 eV has a higher correlation coefficient (0.93), indicating that FeOOH is the primary active site. For nitrogen, the proportions of pyridinic N and pyrrolic N show no significant correlation with the catalytic activity of FeOOH/BC, while the proportions of graphitic N exhibit a good correlation (Fig. S12 in Supporting information).

Therefore, the degradation of CFP was primarily driven by the combined effects of Fe-induced high-valent iron-oxo species and biochar-mediated direct electron transfer.

Cyclic experiments were conducted to investigate the stability of FeOOH/BC further. In the first three cycles, the removal rate of CFP within 20 min remained at 100 %. In the fourth cycle, the removal rate decreased slightly to 97.4 % after 30 min, and in the fifth cycle, the removal rate dropped to 91.4 % (Fig. S13 in Supporting information). During the cyclic tests, the highest iron concentration in the water reached 0.44 mg/L after the first cycle. Subsequently, the concentration of leached iron gradually decreased with each cycle, reaching 0.16 mg/L after the fifth cycle. The results confirmed the good catalytic and structural stability of FeOOH/BC. Based on the previous experiments, the activation of PAA by FeOOH/BC to degrade CFP mainly occurs on its surface. Therefore, the decline in the catalytic activity of FeOOH/BC is likely due to the coverage of CFP and its degradation products on the surface. In this study, FeOOH/BC was regenerated by calcining at 300 °C under nitrogen for 1 h. The regenerated FeOOH/BC was then used to activate PAA to degrade CFP. The results showed that the removal rate of CFP reached 100 % within 20 min, similar to the catalytic performance of fresh FeOOH/BC (Fig. S14 in Supporting information). This further confirmed that the main reaction in the FeOOH/BC/PAA system occurs on the FeOOH/BC surface and provided a method for regenerating FeOOH/BC.

Theoretical calculations were performed to elucidate the reactive sites of CFP. Combined with experimental findings, singlet oxygen ($^1O_2$) was identified as the predominant reactive oxygen species (ROS), exhibiting weak electrophilic characteristics [45]. As shown in Figs. 5a and b, the electrostatic potential (ESP) distribution of the CFP molecule revealed that the pyridine ring and carboxyl group are susceptible to $^1O_2$ attack. The highest occupied molecular orbital (HOMO) and lowest unoccupied molecular orbital (LUMO) analysis (Figs. 5c and d) indicated electron-rich regions localized at the 2S and 7O atoms, which are prone to oxidation by $^1O_2$ [46]. Further evaluation of the Fukui index (Fig. 5e) highlighted the electrophilic reactivity (f^0) of specific atoms: 2S ($f^0 = 0.1149$), 7O ($f^0 = 0.0585$), and 11 N ($f^0 = 0.0318$), consistent with their roles as primary reactive sites. Ultra-high-



Atom	q(N)	q(N+1)	q(N-1)	f^-	f^+	f^0
1(S)	-0.0161	-0.0633	0.0142	0.0303	0.0472	0.0387
2(S)	0.0117	-0.0446	0.1851	0.1734	0.0563	0.1149
3(O)	-0.253	-0.2953	-0.2072	0.0458	0.0423	0.044
4(O)	-0.131	-0.1333	-0.1217	0.0093	0.0023	0.0058
5(O)	-0.1607	-0.1999	-0.1488	0.012	0.0392	0.0256
6(O)	-0.255	-0.3249	-0.2314	0.0235	0.0699	0.0467
7(O)	-0.2902	-0.3248	-0.2079	0.0822	0.0347	0.0585
8(O)	-0.2712	-0.2908	-0.2297	0.0415	0.0196	0.0305
9(N)	-0.0478	-0.0526	-0.0124	0.0354	0.0048	0.0201
10(N)	-0.1068	-0.1121	-0.0846	0.0222	0.0053	0.0137
11(N)	-0.1631	-0.1934	-0.1299	0.0332	0.0304	0.0318
12(C)	0.0258	0.0162	0.0343	0.0085	0.0096	0.0091
13(C)	0.0305	0.0163	0.0416	0.0112	0.0141	0.0126
14(C)	0.1663	0.1333	0.1806	0.0143	0.033	0.0237
15(C)	0.0266	-0.0207	0.0518	0.0253	0.0473	0.0363
16(C)	0.003	-0.0718	0.0434	0.0404	0.0748	0.0576
17(C)	-0.0424	-0.0578	-0.0342	0.0083	0.0154	0.0118
18(C)	0.0348	0.0236	0.0417	0.0069	0.0112	0.009
19(C)	0.2123	0.1582	0.2158	0.0035	0.0541	0.0288
20(C)	0.1615	0.1468	0.1833	0.0218	0.0148	0.0183
21(C)	-0.0462	-0.0615	-0.0249	0.0214	0.0153	0.0183
22(C)	0.2131	0.2042	0.2268	0.0137	0.0089	0.0113
23(C)	-0.0041	-0.0303	0.0006	0.0047	0.0262	0.0154
24(C)	-0.0805	-0.0878	-0.0701	0.0104	0.0073	0.0088
25(C)	-0.0541	-0.0773	-0.0281	0.026	0.0232	0.0246
26(C)	-0.0452	-0.0584	-0.0358	0.0095	0.0131	0.0113
27(C)	0.021	-0.0051	0.0427	0.0217	0.0261	0.0239
28(C)	0.0249	0.0158	0.0397	0.0149	0.0091	0.012

Fig. 5. (a) The geometry of CFP molecule. (b) ESP mapping of CFP. (c) HOMO and (d) LUMO of CFP. (e) Fukui index of CFP. (f) Proposed degradation pathway of CFP in FeOOH/BC activated PAA system.

performance liquid chromatography-mass spectrometry (UHPLC-MS) analysis of transformation products (TPs) confirmed three degradation pathways (Fig. 5f): Pathway I: Oxidation at the 11 N site generated Product **A** (*m/z* 462.11479), which underwent sequential cleavage to yield Product **B** (*m/z* 218.00257) and Product **C** (*m/z* 47.12904), ultimately mineralizing to CO_2/H_2O. Pathway II: Attack at the 2S site formed Product **D** (*m/z* 462.11231), further oxidized to Product **E** (*m/z* 316.40259) and Product **F** (*m/z* 86.10036), followed by complete mineralization. Pathway III: Decarboxylation of the β-lactam ring (19C, $f^0 = 0.0288$) produced Product **G** ($m/z = 403.10356$), which was subsequently converted to Product **H** ($m/z = 174.11250$) and Product **I** ($m/z = 61.00305$), concluding in CO_2/H_2O formation.

In summary, FeOOH/BC exhibits excellent catalytic activity in activating PAA, and its catalytic activity can be modulated by controlling the carbon content in the precursor biochar. When the content of Fe(III) with more hydroxyl groups is higher, FeOOH/BC shows greater catalytic activity toward PAA. The activation of PAA by FeOOH/BC leads to the generation of singlet oxygen, high-valent iron, and surface-active species, with surface-active species playing a dominant role in removing CFP, followed by high-valent iron and singlet oxygen. The iron and nitrogen active sites in FeOOH/BC play a key role in activating PAA. The FeOOH/BC/PAA system also shows excellent resistance to interference from inorganic ions and can effectively remove common organic pollutants in the system. This study provides a novel PAA catalyst, reveals the mechanism by which iron and nitrogen active sites activate PAA, and offers a solution for removing refractory organic pollutants from water.

Declaration of competing interest

The authors declare that they have no known competing financial interests or personal relationships that could have appeared to influence the work reported in this paper.

CRediT authorship contribution statement

Han Yan: Data curation, Writing – original draft. **Xudong Yang:** Methodology, Writing – review & editing. **Wen Liu:** Project administration, Resources. **Fengbin Sun:** Formal analysis, Funding acquisition. **Guodong Jia:** Funding acquisition, Methodology.

Acknowledgments

This work was financially supported by the Beijing Natural Science Foundation (No. 8232035), the National Key R&D Program of China (No. 2024YFF1308200), the multi-dimensional coupling process of soil-surface-subsurface hydrology and vegetation regulation mechanism in loess region (No. U2243202), the National Key R&D Program of China (No. 2021YFA1202500), the Beijing National Laboratory for Molecular Sciences (No. BNLMS2023011). DFT calculations supported by the High-Performance Computing Platform of Peking University and the National Key Scientific and Technological Infrastructure project "Earth System Numerical Simulation Facility" (Earth Lab) are also acknowledged.

Supplementary materials

Supplementary material associated with this article can be found, in the online version, at doi:10.1016/j.cclet.2025.111542.

References

[1] C. Liu, L. Tan, L. Zhang, et al., Front. Env. Sci. 9 (2021) 692298.
[2] Z. Su, K. Wang, F. Yang, et al., Water Res. 235 (2023) 119867.
[3] D.G.J. Larsson, C.F. Flach, Nat. Rev. Microbiol. 20 (2022) 257–269.
[4] M. Tian, X. He, Y. Feng, et al., Antibiotics 10 (2021) 539.
[5] D. Mangla, A. Sharma, S. Ikram, J. Hazard. Mater. 425 (2022) 127946.
[6] X. Wang, J. Jing, M. Zhou, et al., Chin. Chem. Lett. 34 (2023) 107621.
[7] V. Vinayagam, K.N. Palani, S. Ganesh, et al., Environ. Res. 240 (2024) 117500.
[8] B. Liu, B. Huang, X. Ma, et al., J. Environ. Chem. Eng. 12 (2024) 112927.
[9] S. Li, C. Dai, Y. Duan, et al., Sep. Purif. Technol. 330 (2024) 125240.
[10] C. Qiao, W. Jia, J. Tang, et al., Environ. Res. 263 (2024) 120058.
[11] B. Li, Y. Wang, Y. Liu, et al., Chin. Chem. Lett. 36 (2025) 110374.
[12] F. Miao, C. Cheng, W. Ren, et al., Environ. Sci. Technol. 58 (2024) 8554–8564.
[13] Z. Wang, Z. Chen, Q. Li, et al., Environ. Sci. Technol. 57 (2023) 10478–10488.
[14] T. Li, Y. Yu, M. Pei, J. Phys. Chem. C 127 (2023) 6271–6279.
[15] X. Li, Y. Fu, S. Zhao, et al., Chem. Eng. J. 430 (2022) 133101.
[16] Y. Gong, Y. Wang, N. Lin, et al., Environ. Pollut. 299 (2022) 118871.
[17] H.K. Thejas, N. Hossiney, Mater. Today: Proc 61 (2022) 327–331.
[18] M.A. Shaida, S. Verma, S. Talukdar, et al., J. Mol. Liq. 374 (2023) 121259.
[19] J. Lu, Q. Lu, L. Di, et al., Chin. Chem. Lett. 34 (2023) 108357.
[20] F. Amalina, A.S. Abd Razak, S. Krishnan, et al., J. Hazard. Mater. Adv. 7 (2022) 100134.
[21] S. Haghighi Mood, M.R. Pelaez-Samaniego, M. Garcia-Perez, Energ. Fuel. 36 (2022) 7940–7986.
[22] M. Sadatsharifi, M. Purgel, Struct. Chem. 35 (2024) 961–966.
[23] M.S. Alenezi, Y.H. Tartor, M. El-Sherbini, et al., Antibiotics 13 (2024) 1073.
[24] C. Li, A. Li, X. Hui, et al., Ecotoxi. Environ. Safe. 285 (2024) 117022.
[25] C. Chi, Z. Liu, G. Wang, et al., Adv. Energy Mater. 13 (2023) 2302055.
[26] S.S. Sahoo, V.K. Vijay, R. Chandra, et al., Clean. Eng. Technol. 3 (2021) 100101.
[27] Y. Teng, X.D. Wang, J.F. Liao, et al., Adv. Funct. Mater. 28 (2018) 1802463.
[28] S. Zhang, H. Gao, Y. Huang, et al., Enviro. Sci.: Nano 5 (2018) 1179–1190.
[29] N. Song, B. Xi, P. Wang, et al., Nano Res. 15 (2022) 1424–1432.
[30] M. Cao, X. Zhao, X. Gong, Small 18 (2022) 2106683.
[31] G. Ye, S. Liu, K. Zhao, et al., Angew. Chem. 135 (2023) e202303409.
[32] T.J. Frankcombe, Y. Liu, Chem. Mater. 35 (2023) 5468–5474.
[33] S. Yin, Y. Gao, L. Chen, et al., Sci. China. Technol. *Sc.* 67 (2024) 3103–3115.
[34] S. Jiao, M. Liu, Y. Li, et al., Carbon 193 (2022) 339–355.
[35] T. Zhang, Y. Wen, Z. Pan, et al., Environ. Sci. Technol. 56 (2022) 2617–2625.
[36] J. Wu, J. Zou, J. Lin, et al., Environ. Sci. Technol. 58 (2024) 15741–15754.
[37] C. Dai, S. Li, Y. Duan, et al., Water Res. 216 (2022) 118347.
[38] X. Peng, Z. Fan, Q. Wang, et al., Sep. Purif. Technol. 345 (2024) 127365.
[39] L.V. de Faria, R.G. Rocha, L.C. Arantes, et al., Electrochim. Acta 429 (2022) 141002.
[40] Y. Liu, Y. Zhang, L. Zhang, et al., Chem. Eng. J. 490 (2024) 151585.
[41] H. Zhao, Y. Ren, C. Liu, et al., J. Hazard. Mater. 459 (2023) 132117.
[42] F. Yu, C. Li, W. Li, et al., Adv. Funct. Mater. 34 (2024) 2307230.
[43] S. Li, Y. Yang, H. Zheng, et al., Water Res. 225 (2022) 119176.
[44] G. Song, R. Gao, Z. Zhao, et al., Appl. Catal. B: Environ. 301 (2022) 120809.
[45] B.Y. Huang, L. Chen, M.W. Cao, et al., Sep. Purif. Technol. 330 (2024) 125539.
[46] W. Yang, J. Yi, W. Sun, Macromol. Chem. Phys. 216 (2015) 1125–1133.